Front. Chem. Sci. Eng. 2022, 16(9): 1345−1354
https://doi.org/10.1007/s11705-022-2155-1

RESEARCH ARTICLE

Tuning porosity of coal-derived activated carbons for CO_2 adsorption

Zhipeng Qie[1,2], Lijie Wang[3], Fei Sun (✉)[1], Huan Xiang[4], Hua Wang[1], Jihui Gao[1], Guangbo Zhao[1], Xiaolei Fan[2]

1 School of Energy Science and Engineering, Harbin Institute of Technology, Harbin 150001, China
2 Department of Chemical Engineering and Analytical Science, The University of Manchester, Manchester M13 9PL, UK
3 China Datang Corporation Renewable Energy Science and Technology Research Institute, Beijing 100052, China
4 Energy and Bioproducts Research Institute (EBRI), Aston University, Birmingham B4 7ET, UK

Abstract A simple method was developed to tune the porosity of coal-derived activated carbons, which provided a model adsorbent system to investigate the volumetric CO_2 adsorption performance. Specifically, the method involved the variation of the activation temperature in a K_2CO_3 induced chemical activation process which could yield activated carbons with defined microporous (< 2 nm, including ultra-microporous < 1 nm) and meso-microporous structures. CO_2 adsorption isotherms revealed that the microporous activated carbon has the highest measured CO_2 adsorption capacity (6.0 mmol·g^{-1} at 0 °C and 4.1 mmol·g^{-1} at 25 °C), whilst ultra-microporous activated carbon with a high packing density exhibited the highest normalized capacity with respect to packing volume (1.8 mmol·cm^{-3} at 0 °C and 1.3 mmol·cm^{-3} at 25 °C), which is significant. Both experimental correlation analysis and molecular dynamics simulation demonstrated that (i) volumetric CO_2 adsorption capacity is directly proportional to the ultra-micropore volume, and (ii) an increase in micropore sizes is beneficial to improve the volumetric capacity, but may lead a low CO_2 adsorption density and thus low pore space utilization efficiency. The adsorption experiments on the activated carbons established the criterion for designing CO_2 adsorbents with high volumetric adsorption capacity.

Keywords coal-derived activated carbons, porosity, CO_2 adsorption, molecular dynamics

1 Introduction

Serious environmental problems (such as acid rain, haze and greenhouse gases) have arisen due to the widespread use of fossil fuels. Especially, the sharp rise of concentration of CO_2 from ca. 325 ppm (1967) to 409.8 ppm (2019) has aroused wide public concern [1,2]. Nowadays, several chemical absorption and/or physical adsorption technologies (based on membranes [3,4], alkanol amine solvents [5], ionic liquids [6] and solid adsorbents [7,8]) have been used for CO_2 capture and storage. Among them, CO_2 adsorption by solid adsorbents is considered one of the most promising technologies due to low energy requirement, good stability and relatively wide operation ranges of temperatures and pressures. Solid adsorbents mainly include carbon-based materials [9,10] zeolites [11], metal-organic frameworks [12] and amine functionalized/supported adsorbents [13]. Among them, carbon-based materials have been widely explored and applied in CO_2 capture due to their favorable properties of high adsorption capacity, superior cycle stability, adjustable pore structures and, more importantly, reasonable costs. For example, coal/biomass-based activated carbons (ACs) are common adsorbents which are derived from low-cost raw materials and can be produced at scales. Among various approaches for preparing ACs, chemical activation using KOH [14], K_2CO_3 [15], H_3PO_4 [16] and NaOH [17] is commonly employed, as well as being practical for applications at scales. Especially, K_2CO_3 is more environmentally friendly compared to hazardous KOH and NaOH, but being comparable regarding its performance for activation. Yue et al. [18] investigated the activation of coconut shell using K_2CO_3, and the optimized microporous sample showed a high CO_2 capacity of 3.71 mmol·g^{-1} at 25 °C and 5.12 mmol·g^{-1} at 0 °C. Kim et al. [19] prepared a series of coffee ground-based microporous carbons using K_2CO_3 activation, which also showed good CO_2 uptakes, proving that K_2CO_3 activation was capable of producing high-performance CO_2 adsorbents.

Received August 29, 2021; accepted December 22, 2021

E-mail: sunf@hit.edu.cn

Textural and surface chemical properties of ACs are key to determine their performance for CO_2 capture. In this regard, continuous efforts have been made to tune the pore structure and surface functionality of ACs to improve their CO_2 adsorption performance. It is generally agreed that CO_2 adsorption on ACs is based on a micropore filling mechanism, and the CO_2 adsorption capability of ACs is mostly related to narrow micropore structure [20]. Previous studies have demonstrated micropores with sizes smaller than 1 nm, i.e., ultra-micropores, are mainly responsible for CO_2 uptake at ambient pressure [21,22]. Additionally, chemical environment of ACs is also an important factor of affecting CO_2 adsorption, which can induce chemisorption, hydrogen bonding, and/or electrostatic interactions between the CO_2 molecule and surface functional groups [23,24]. The porosity of ACs can be effectively adjusted by carbon precursors [25] and activation methods [26], as well as the conditions of the method [27]. Based on pore adjustment and surface modification, CO_2 adsorption capabilities of the reported ACs have been significantly increased, and some of the reported ACs with the appropriate pores and active sites could achieve the CO_2 adsorption capacity of > 7 mmol·g^{-1} at 0 °C and 1 bar [28]. However, it is worth mentioning that the majority of previous studies focused mainly on improving the CO_2 gravimetric capacitive performance of porous carbons with the low packing density, which could cause the insufficient use of pores in ACs. Conversely, in comparison with the gravimetric performance, CO_2 adsorption capability per volume of porous carbons may provide a relatively realistic indication of the performance. Besides, the volumetric CO_2 adsorption capability of porous carbons is also an important indicator to determine the scale and efficiency of adsorption systems [29–31], which, however, was commonly overlooked in most of the previous studies [20,32]. To achieve a high volumetric CO_2 adsorption capacity, porosity regulation of carbon materials is the prerequisite since pore configuration and size greatly correspond to the packing density of porous carbons [33]. Regardless gravimetric and volumetric adsorption, it is very necessary to explore the critical factors, which determine volumetric and/or gravimetric capability of porous carbons, and hence devise controllable methods for porosity regulation towards high-performance CO_2 adsorbents.

Here, we report a simple chemical activation method using K_2CO_3 as the activating agent to prepare coal-derived ACs. By simply varying the activation temperature (in a range of 600–900 °C), the porosity of the resulting ACs can be tailored. Specifically, the low-temperature (at 600 °C) activation produced the AC with mainly ultra-micropores (< 1 nm), whilst an increase in the activation temperature can increase the pore sizes. The series ACs obtained can be used as a model adsorbent system for investigating the correlation between pore parameters and volumetric CO_2 adsorption characteristics. Based on the combined experimental study and molecular dynamics simulation, the correlation between the CO_2 adsorption capacity and pore characteristics of the ACs is proposed.

2 Experimental

2.1 Preparation of ACs

To prepare the ACs, a low-rank coal from Xinjiang province (China) was used as the carbon source, and the proximate, ultimate analyses, ash compositions of the coal are presented in Tables S1 and S2 (cf. Electronic Supplementary Material, ESM). The activation of the coal precursor towards ACs is illustrated in Fig. 1. In detail, coal particles (< 1 mm) were first washed using acids (mixture of 5 mol·L^{-1} hydrochloric acid and 20 wt% hydrofluoric acid) to remove the minerals. To prepare ACs, the acid-washed coal particles were added into 0.2 g·mL^{-1} K_2CO_3 solution with a mass ratio of 1:3 to form the coal-water slurry under magnetic stirring. The mixture was then evaporated at 100 °C to obtain the dry solid and further carbonized at the setting temperature for 1 h under nitrogen atmosphere (200 mL·min^{-1}) at a heating rate of 5 °C·min^{-1} in a horizontal tube furnace, as shown in Fig. S1 (cf. ESM). After activation, the sample was washed using 2 mol·L^{-1} hydrochloric acid and deionized water (three times) sequentially, and then dried at 80 °C for 12 h to obtain the ACs. The resulting ACs were denoted as AC-600, AC-700, AC-800 and AC-900 for the activation temperatures of 600, 700, 800, 900 °C, respectively.

2.2 Structural characterization and CO_2 adsorption

The morphology, microstructure and element composition of the obtained ACs were characterized by scanning electron microscopy (SEM, Helios Nanolab600i) and transmission electron microscopy (TEM, JEM-2100, at 200 kV). Porous properties of the ACs including specific surface area, pore volume and pore size distribution were measured by N_2 adsorption/desorption analysis (Micromeritics ASAP 2020 adsorption analyzer) at liquid nitrogen temperature (–196 °C). Before the test, ACs samples were degassed at 160 °C for 8 h. Specifically, the Brunauer–Emmett–Teller (BET) theory was used to determine the specific surface area (S_{BET}); the total pore volume (V_{total}) was determined using the amount adsorbed at relative pressure (p/p^0) of 0.975; the ultra-micropore ($\leqslant$ 1 nm) volume ($V_{(\leqslant 1\ nm)}$) are calculated using the density functional theory (DFT) model, i.e., the accumulated pore volume with pore size less than 1 nm [34]. X-ray diffraction (XRD) patterns of materials were collected

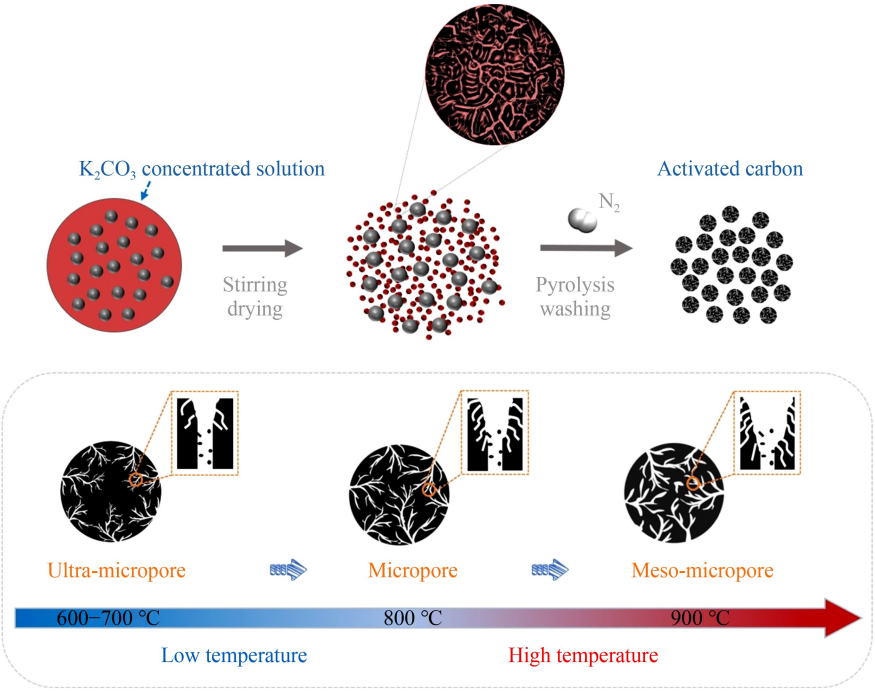

Fig. 1 Schematic K_2CO_3 activation of the coal precursor to prepare ACs, and the associated pore formation process in the ACs.

using a Rigaku D/Max 2400 diffractometer with CuKα radiation (40 kV, 40 mA, λ = 1.5406 Å). The packing density of the ACs ($d_{packing}$) was defined as the mass per unit volume measured after packing the AC samples in a 10 mL measuring cylinder by vibration method, in which the frequency was 120 min^{-1} and the amplitude was 3 mm. CO_2 adsorption on the ACs was conducted using the Micromeritics ASAP 2020 adsorption analyzer at 0 and 25 °C to obtain the isotherms in a pressure range of 0 to 1 bar, and the CO_2 adsorption capacity directly acquired from this instrument was denoted as q. Before CO_2 adsorption, the ACs samples were degassed at 180 °C under N_2 for 8 h.

2.3 Molecular dynamics simulation

In this study, the 3-layer graphitic slit-pore models with different pore sizes were used to simulate CO_2 adsorption on the ACs [35,36]. The effective pore sizes (D_{eff}) were selected as 0.2, 0.4, 0.6, 0.9, 2.0 and 3.5 nm, and the actual pore spaces (D_{act}) were calculated by $D_{act} = D_{eff} +$ 0.335 nm correspondingly, where 0.335 nm is the layer distance of graphite. The structure file (.pdb) of CO_2 molecule was built by Gview (GaussView 5.0). The corresponding topology file (.itp) and relevant parameters of CO_2 molecule in the forcefield file (such as C–O bond length and atom charge) were obtained from the automated topology builder online molecular library [37]. The topology file of CO_2 molecule was optimized using DFT at B3LYP 6-31(G) level. Graphite laminates were created by visual molecular dynamics software. Here we used the command x2top in GROMOS 54A7 to generate the topology file of the graphene-like structure. Specifically, the atomic type was aromatic carbon CR1, and the standard C–C bond length was 0.142 nm [38]. All simulations in this work were performed in the NVT ensemble (i.e., the number of particles N, the volume V and the temperature T of the system were kept constant), and a V-RESCALE thermostat method was used to maintain the system temperature with a relaxation constant of 1.0 ps. In Gromos force field, non-bonded force dominates the interactions between gas molecules and the inner wall of carbon slit pore, which is based on Lennard–Jones potential. Van der Waals interactions were calculated using the cut-off method within a cut-off distance of 1.0 nm, and the smooth particle-mesh Ewald method was employed to account for the long-range electrostatic interactions. The total simulation time is 10 ns for each system with an integration time step of 1 fs, which is sufficient to achieve the balance of total energy of the simulation system.

3 Results and discussion

3.1 Coal-derived ACs and their structural characteristics

During the activation with K_2CO_3, carbonization of the coal precursor with the main reactions of $K_2CO_3 + C \leftrightarrow K_2O + 2\ CO$ and $K_2O + C \leftrightarrow 2\ K + CO$ are expected at elevated temperatures, to form ACs with various pore structures, as illustrated in Fig. 1. An increase in the activation temperature caused the variation in pore sizes of the ACs, which was evidenced by the N_2 adsorption/

desorption analysis. Figure 2 and Table 1 show the corresponding pore size distributions and detailed pore parameters of prepared ACs, which exhibit significant differences.

N_2 adsorption/desorption isotherms of the ACs are shown in Fig. 2(a), in which the ACs obtained at low activation temperatures of < 900 °C show the typical Type I adsorption/desorption isotherms with predominant N_2 uptake at $p/p^0 > 0.1$, that is, microporous structures. Conversely, AC-900 exhibits the IV isotherm with a hysteresis loop at $0.45 < p/p^0 < 1.0$, which suggests the presence of mesopores [39]. The N_2 amount adsorbed on the ACs (Fig. 2(a)), the BET surface area and pore volumes of the ACs (Table 1) showed the strong dependence on the activation temperature. In detail, S_{BET} and V_{total} of AC-600 were the lowest at about 415 $m^2 \cdot g^{-1}$ and 0.22 $cm^3 \cdot g^{-1}$, respectively. By increasing the activation temperature to 700 and 800 °C, S_{BET} was enhanced to about 636 and 941 $m^2 \cdot g^{-1}$ for AC-700 and AC-800, respectively. For AC-900, its S_{BET} and V_{total} were the highest among the ACs under investigation at 1592 and 0.95 $m^2 \cdot g^{-1}$, respectively. DFT pore size distributions (PSDs) of the ACs are shown in Fig. 2(b), which show that all the ACs possess ultra-micopores of 0.6–0.9 nm and micropores of about 1.3 nm. By increasing the activation temperature to 900 °C, in addition to the ultra-micopores and micropores, development of larger pores was observed to have the PSD at 1.5–5 nm, which extended into the mesopores. It is also worth noticing that, with an increase in the activation temperature, the PSD of the ACs shifted slightly to the right. For example, in the ultra-microporous range (i.e., < 1 nm), PSD of AC-600 centered at ca. 0.7 nm, whiles that of AC-800 shifted to 0.8 nm. Also, the intensity of differential PSDs increased as well as a function of the activation temperature, which suggests the expansion of pore volume, being in line with the specific pore volume data (Table 1). To demonstrate this further, a ratio of ultra-micropore volume to total pore volume ($V_{(\leqslant 1\ nm)}/V_{total}$) was defined, which represent the proportion of ultra-micropores in the porous network of the ACs, as shown in Table 1. Clearly, a continuous decrease of the $V_{(\leqslant 1\ nm)}/V_{total}$ ratio was found from 0.95 (for AC-600) to 0.48 (for AC-900) as a function of activation temperature from 600 to 900 °C. In summary, based on the discussion above, variation of the temperature of the K_2CO_3 activation of the coal precursor created a series of ACs with different porous properties, which can serve as a model adsorbent system for exploring the relationship between the pore structure and CO_2 adsorption performance.

As shown in Fig. 3, more characterization methods were employed to investigate the properties of ACs. Figures 3(a)–3(h) show SEM and TEM micrographs of the ACs under investigation, and all the ACs show uneven surfaces with wrinkles inherited from the parent. Comparatively, the ACs obtained from relatively high activation temperatures, i.e., AC-800 and AC-900, show the presence of surface cracks (dotted frames in Figs. 3(e) and 3(g)) compared with AC-600 (Fig. 3(c)), which could be due to the severer carbonization reactions at higher temperatures. TEM characterisation of the AC-600/700/800 (Figs. 3(b), 3(d) and 3(f)) show that these AC samples have similar amorphous microstructures dominated by micropores. In comparison, TEM image of AC-900 also suggests the presence of local long-range ordered graphene-like structures, which might be associated with

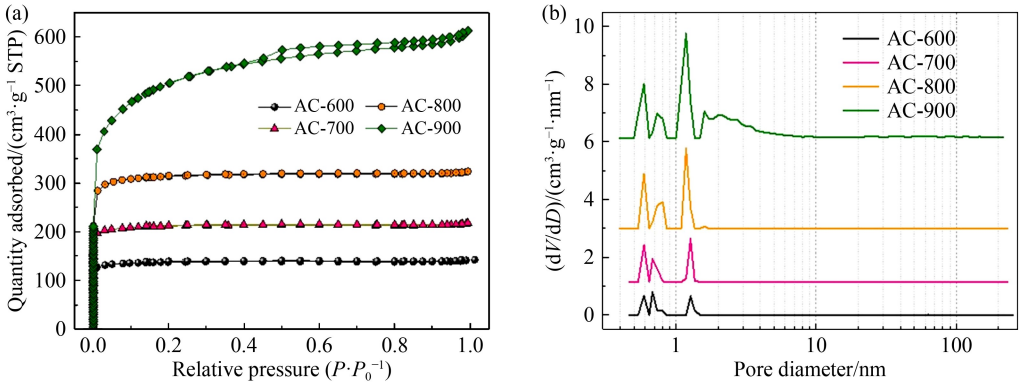

Fig. 2 (a) N_2 adsorption/desorption isotherms and (b) DFT pore size distribution of the ACs.

Table 1 Textural properties of the ACs under investigation

Sample	$S_{BET}/(m^2 \cdot g^{-1})$	$V_{total}/(cm^3 \cdot g^{-1})$	$V_{(\leqslant 1\ nm)}/(cm^3 \cdot g^{-1})$	$V_{(\leqslant 1\ nm)}/V_{total}$
AC-600	415	0.22	0.20	0.95
AC-700	636	0.34	0.30	0.88
AC-800	941	0.50	0.40	0.82
AC-900	1592	0.95	0.46	0.48

the formation of potassium-carbon complex at high activation temperatures, as reported in our previous work [39,40].

Raman spectroscopy and XRD analyses of the ACs, and the results are shown in Figs. 3(i)–3(j). Raman spectra of the ACs (Fig. 3(i)) exhibit the two peaks at 1350 and 1596 cm^{-1}, respectively, which represent the D band of sp^2 carbon atoms with defects and G band of planar sp^2-configured carbon atoms, and are typical for the amorphous carbon structure of the ACs. XRD patterns of the ACs (Fig. 3(j)) show some differences, that is, AC-600 and AC-700 exhibit two broad diffraction peaks at ca. 23° and 43°, which can be assigned to the (002) and (100) planes of amorphous carbon, being in good agreement with the amorphous structures shown in TEM images (i.e., Figs. 3(b) and 3(d)). As compared with AC-600 and AC-700, the diffraction peaks of the (002) and (100) planes in AC-800 and AC-900 were less obvious. This should be ascribed to the well-developed porosity, which was also reported in the previous study on developing porous carbons [34].

3.2 CO_2 adsorption on the ACs

Figure 4 illustrates CO_2 adsorption performance of the ACs developed by this work. As shown in Fig. 4(a) and Fig. S2 (cf. ESM), CO_2 adsorption isotherms were measured at 0 and 25 °C, respectively. All adsorption experiments were conducted with the cut-off pressure of 1 bar. As one can see in Fig. 4(a), at 0 °C, isotherms of AC-600 and AC-700 leveled off with an increase in adsorption pressure, which suggest that CO_2 adsorption on them was approaching the equilibrium. Conversely, that of AC-800 and AC-900 increased continuously with an increase in pressure. The findings are in good agreement with the porous property of the ACs, that is, the enhanced pore volume of the ACs with an increase in the activation temperature. Interestingly, at the end of the adsorption analysis (at 1 bar), the measured CO_2 adsorption capacity (q) of AC-800 was the highest (i.e., 6.0 $mmol \cdot g^{-1}$ at 0 °C and 4.1 $mmol \cdot g^{-1}$ at 25 °C), rather than AC-900, which has the highest S_{BET} and V_{total} values, as well as mesopores. Such findings suggest that the micro-mesopore network in AC-900 might not be hierarchical, which could hinder the uptake of CO_2 molecules during adsorption assessment. This can be proved by examining the slopes of adsorption isotherms of AC-800 and AC-900. Specifically, from 0 to 1 bar, the increasing rate of CO_2 uptake of AC-800 is 6.1 $mmol \cdot g^{-1} \cdot bar^{-1}$, which is much higher than that of the AC-900

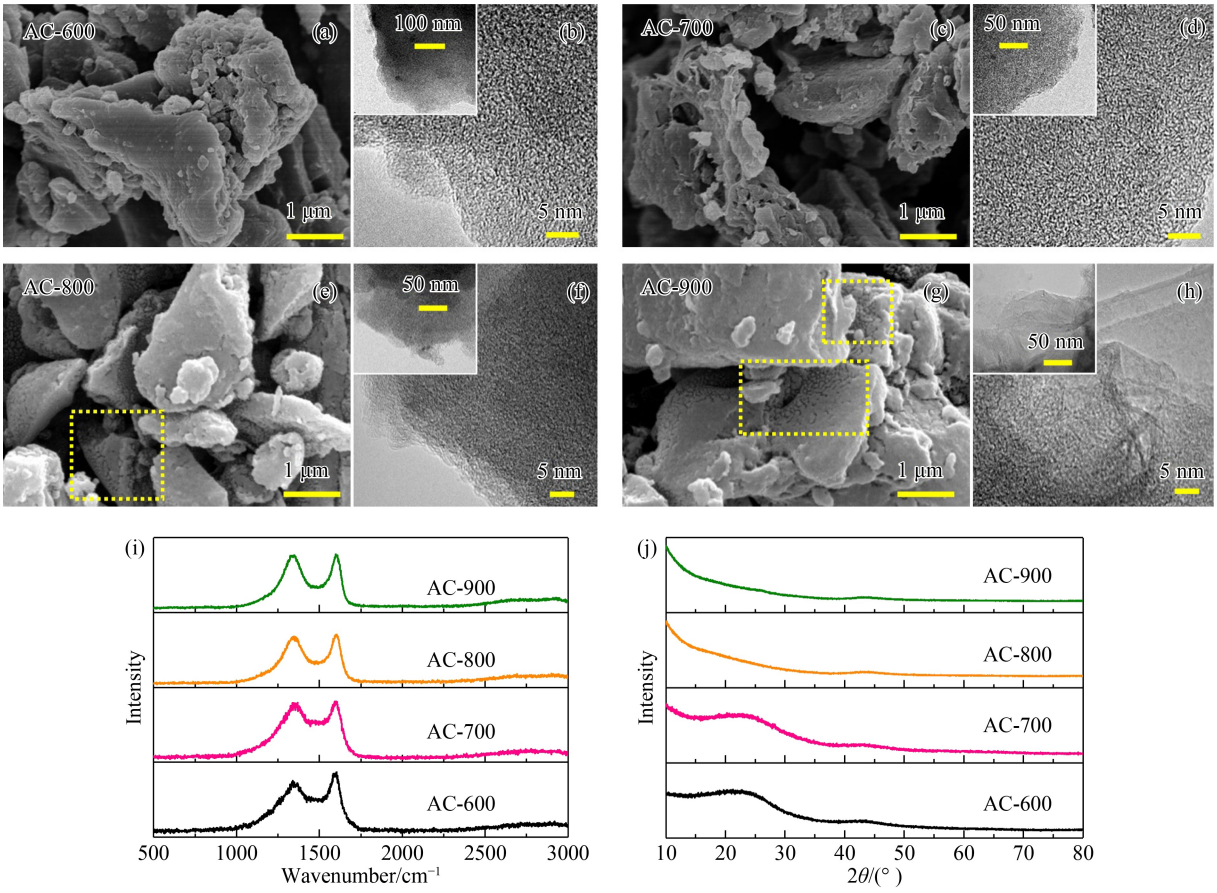

Fig. 3 (a) SEM and (b) TEM images of AC-600; (c) SEM and (d) TEM images of AC-700; (e) SEM and (f) TEM images of AC-800; (g) SEM and (h) TEM images of AC-900; (i) Raman spectra of the ACs; (j) XRD patterns of the ACs.

(4.7 mmol·g^{-1}·bar^{-1}). One possible explanation for the relatively poor CO_2 adsorption of AC-900 is the possible creation of slit-shaped ink-bottle pores or closed-end slit pores at 900 °C. Although AC-900 has the highest specific surface area and pore volume, its CO_2 adsorption capacity was still poor compared to AC-800, which is mainly microporous with the $V_{(\leqslant 1\ nm)}/V_{total}$ ratio of 0.82. Similar adsorption performance was also measured at 25 °C, as shown in Fig. S2. Regarding the microporous ACs (i.e., AC-600/700/800), the measured CO_2 adsorption performance corresponds to their pore characteristics well. Importantly, as the best-performed material under investigation, the capacity of AC-800 is much higher than that reported for other coal/biomass-based ACs, as shown in Table S3 (cf. ESM).

Figure 4(b) shows the packing patterns of the ACs (with the mass of ca. 150 mg), which suggest the difference in the packing density of the ACs. The calculated packing densities of the ACs ($d_{packing}$) are 0.45 g·cm^{-3} (AC-600), 0.23 g·cm^{-3} (AC-700), 0.17 g·cm^{-3} (AC-800) and 0.11 g·cm^{-3} (AC-900). Accordingly, measured CO_2 adsorption capacity (q) was corrected using the packing density to obtain the adsorption capacity of packing bed (i.e., $q_{cv,d} = q \times d_{packing}$) and normalized with respect to S_{BET} (i.e., $q_{sv,BET}$) and V_{total} (i.e., $q_{sv,Vt}$) the to further understand their CO_2 adsorption behaviors (all the calculated values of $q_{cv,d}$, $q_{sv,BET}$ and $q_{sv,Vt}$ are presented in Table 2 and Fig. S3 (cf. ESM)). Figure 4(c) shows the calculated $q_{cv,d}$ values of the ACs, in which AC-600 exhibits the highest value of 1.8 mmol·cm^{-3}. Therefore, considering the scenario for practical applications, especially industrial fixed adsorption beds/towers for dealing with a large amount of gaseous pollutants, ACs with the high packing density have the potential to achieve a high CO_2 capacity with the reduced reactor volume.

The correlation between the measured CO_2 adsorption capacity (q) and the total pore volume of the ACs (V_{total}) is shown in Fig. 4(d), which shows that there is positive linear relationship between the q values of the microporous ACs (i.e., AC-600/700/800) and their total pore volumes. Conversely, for the meso-micro-porous AC-900, although it has the highest V_{total} value, the distribution of its q value deviated significantly from the linear correlation of AC-600/700/800. This again proves that the pore volume of the meso-micro-porous AC-900 was not fully utilized during CO_2 adsorption at 0 °C. The specific

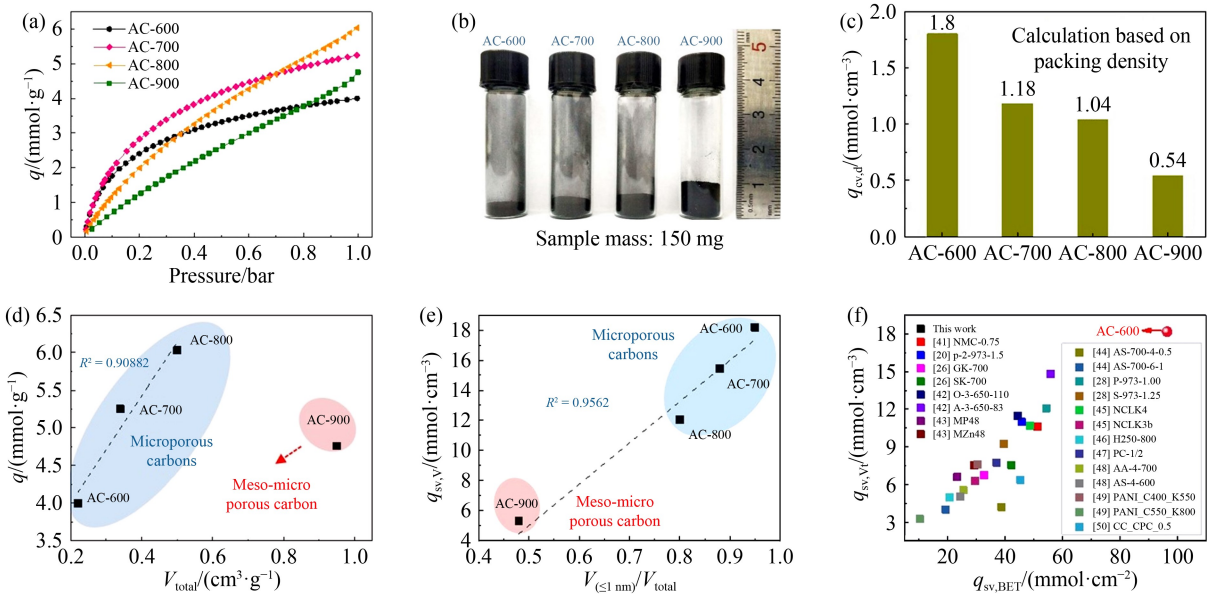

Fig. 4 (a) CO_2 adsorption isotherms of the ACs measured at 0 °C; (b) photos of the packing patterns of the ACs at ca. 150 mg; (c) packing density ($d_{packing}$) corrected volumetric CO_2 adsorption capacities ($q_{cv,d}$) of the ACs at 0 °C and 1 bar; (d) q–V_{total} correlation of the ACs at 0 °C and 1 bar; (e) $q_{sv,Vt}$–($V_{(\leqslant 1\ nm)}/V_{total}$) correlation of the ACs at 0 °C; (f) comparison of $q_{sv,Vt}$ and $q_{sv,BET}$ values of different biomass/coal-derived ACs with AC-600 for CO_2 adsorption at 0 °C.

Table 2 CO_2 adsorption capacities at 0 °C of the ACs under investigation

Sample	q [a)]/(mmol·g^{-1})	$q_{cv,d}$/(mmol·cm^{-3})	$q_{sv,BET}$/(mmol·cm^{-2})	$q_{sv,Vt}$/(mmol·cm^{-3})
AC-600	4.1	1.8	96.4	18.2
AC-700	5.3	1.2	82.6	15.4
AC-800	6.0	1.0	64.1	12.1
AC-900	5.0	0.5	31.5	5.3

a) q values in this table are selected from Fig. 4(a) at the condition of 0 °C and 1 bar.

CO_2 adsorption capacities ($q_{sv,Vt}$) of the ACs were further correlated with the $V_{(\leqslant 1\ nm)}/V_{total}$ ratio, as shown in Fig. 4(e). A linear relationship was established for all the ACs, which shows the increase of $q_{sv,Vt}$ values as an increase in the $V_{(\leqslant 1\ nm)}/V_{total}$ ratio for the ACs under investigation. The addition analysis clearly demonstrates that, during CO_2 adsorption at 0 °C, packing of CO_2 molecules was preferably in the ultra-micropores of the ACs. In addition, it also suggests that an increase in the activation temperature caused the formation of ink-bottle or closed-end slit mesopores, which was not desirable for CO_2 adsorption since the mesopore and/or micropore volumes in the ACs could become inaccessible after the occupation of ultra-micropores. Same practice was conducted for the adsorption data at 25 °C (Table S4, cf. ESM), and same conclusions were drawn as shown by the findings presented in Fig. S4 (cf. ESM).

Figure 4(f) presents the $q_{sv,Vt}$–$q_{sv,BET}$ plots of various reported porous carbons [20,26,28,41–50] in comparison with AC-600 which has shown the best CO_2 adsorption performance (on the basis of $q_{sv,Vt}$) due to its well-developed ultra-micropore structure. One can see that the developed AC-600 outperformed the state-of-the-art materials regarding both the CO_2 adsorption per total pore volume and BET surface area, which suggests the very efficient use of its micropore space for packing CO_2 molecules and the great potential for being adopted by industrial adsorption systems for practical CO_2 capture. Further comparison based on $q_{sv,Vt}$ and $q_{sv,BET}$ values is presented in Table S3, again AC-600 demonstrated the best performance. To assess the selectivity of the developed ACs, AC-800 with the highest measured CO_2 capacity was selected to perform N_2 adsorption at 0 °C. Figure S5 (cf. ESM) compares the relevant N_2 and CO_2 isotherms. At 1 bar, the measured N_2 adsorption capacity of AC-800 was 1.17 mmol·g^{-1}, which was much lower than the measured CO_2 adsorption capacity of AC-800, suggesting the good selectivity to CO_2 adsorption against N_2 for the developed ACs.

3.3 Molecular dynamics simulation

To further investigate the correlations between pore parameters of ACs and CO_2 adsorption performance, molecular dynamics simulation was carried out based on the typical 3-layer slit pore models, and relevant results were summarized and shown in Fig. 5. Figure 5(a) shows snapshots of the simulation system when the total energy reaches equilibrium, from which it can be found that: (i) pores with effective size (D_{eff}) smaller than the diameter of CO_2 molecule (i.e., 0.33 nm) have no CO_2 capacity; (ii) in the pore with D_{eff} = 0.4 nm, mono-layer CO_2 adsorption dominates to give the highest local density (205 kg·m^{-3}) and overall number density (24.60 nm^{-3}) as shown in the narrow peak of Fig. 5(b); (iii) in the pore with D_{eff} = 0.6 nm, double-layer CO_2 adsorption exists with a local density of 128 kg·m^{-3} in each layer. Interestingly, the CO_2 layer density in ultra-micro pores is close to the magnitude of liquid (e.g., water density is 997 kg·m^{-3} under standard condition), which indicates the dense adsorption of CO_2; (iv) in the pores with D_{eff} > 2.0 nm,

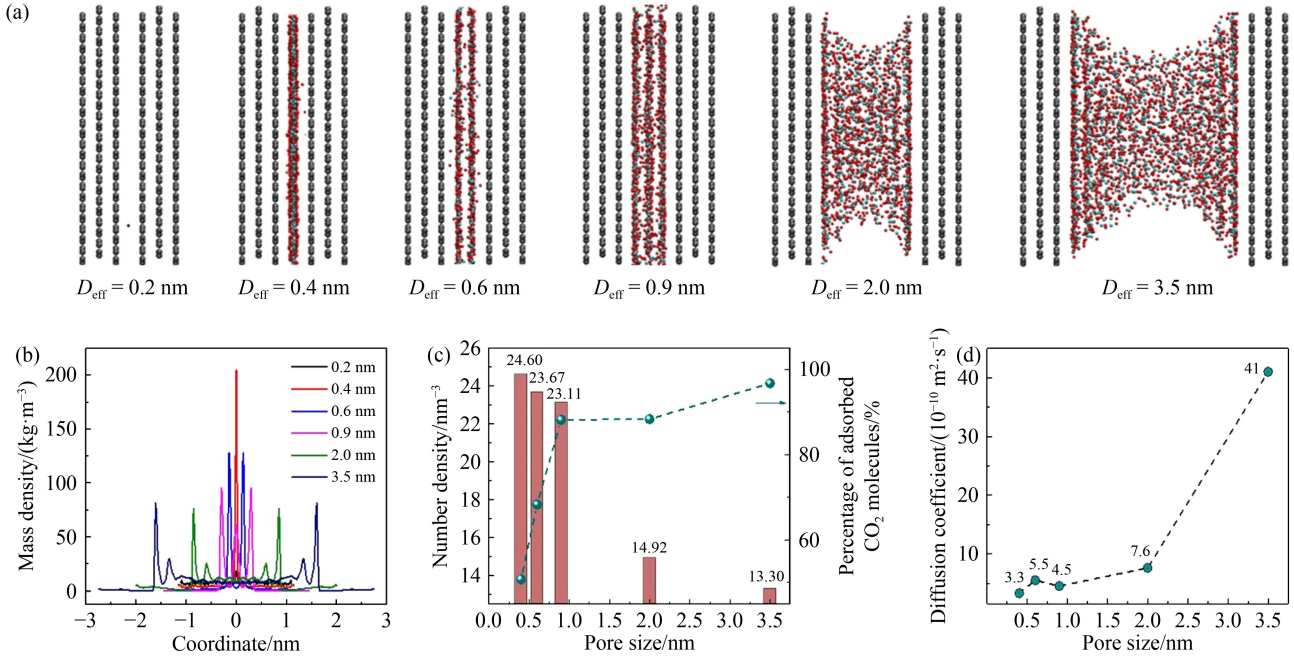

Fig. 5 (a) CO_2 adsorption on AC models of different effective pore sizes; (b) density profiles of CO_2 molecules along the pores with pore diameters ranging from 0.2 to 3.5 nm; (c) number density and percentage of CO_2 molecules adsorbed inside the slit pore; (d) self-diffusion coefficients of CO_2 in pores with different effective sizes.

multi-layer adsorption appears, in which only the layers close to the pore wall show high density, whilst the CO_2 molecules in the outer layers are loosely packed with insignificant density peaks, as shown in Fig. 5(b). Thus, based on the simulation results, the ultra-micropores possess extremely high CO_2 adsorption density as compared to mesopores, which is the microscopic explanation of the positive correlation between volumetric capacity $q_{sv,Vt}$ and the volume of ultra-micro pores (i.e., $V_{(\leqslant 1\ nm)}$). In addition, as shown in Fig. 5(c) and Table S5 (cf. ESM), the overall CO_2 density shows a dramatic fall as the pore size increases from 1 nm to 2 nm, which corresponds with the drop of $q_{sv,Vt}$ between AC-800 and AC-900 as listed in Table 2.

Molecular dynamics simulation also suggested that an increase in pore sizes provides sufficient space to allow the transportation of CO_2 molecules, and thus the self-diffusion coefficient of CO_2 molecules in the slit pore space increases (Tables S5–S6 (cf. ESM) and Fig. 5(d)). This verifies the conclusion that the measured CO_2 capacities (q) increase linearly with the total pore volumes (i.e., Fig. 4(d)). However, based on this model, it is difficult to explain the result that meso-micro porous AC-900 has relatively lower measured CO_2 capacity (q) than microporous AC-800, which may be due to the developed ink pore structure of AC-900 as discussed above.

4 Conclusions

In summary, a facile chemical activation method was developed (by simply varying the temperature of K_2CO_3 solution) to convert coal to ACs with the controlled porosity, i.e., microporous and meso-micro porous ACs with different proportion of ultra-micropores (< 1 nm). The obtained ACs were used as model adsorbents to study the relationship between CO_2 adsorption capacity and porosity of ACs, which revealed the importance of ultra-micropores of the ACs for CO_2 uptake. Sample AC-800 (i.e., activation at 800 °C) possesses the highest measured CO_2 adsorption capacity (6.0 mmol·g^{-1} at 0 °C and 4.0 mmol·g^{-1} at 25 °C), while AC-600 shows the highest volumetric capacity normalized with respect to packing volume (1.8 mmol·cm^{-3} at 0 °C and 1.3 mmol·cm^{-3} at 25 °C) and total pore volume (18.2 mmol·cm^{-3} at 0 °C and 12.8 mmol·cm^{-3} at 25 °C), which are among the highest levels of reported ACs. Both experimental results and molecular dynamics simulation demonstrate that the measured CO_2 adsorption capacities increase linearly with the pore volume of microporous carbons while CO_2 volumetric capacities are directly proportional to the ultra-micropore volume. This work offers a design principle towards solid porous adsorbents with high CO_2 volumetric or specific capability of packing bed.

Acknowledgements This work was financially supported by the National Natural Science Foundation of China (Grant No. 51806050) and the Fundamental Research Funds for the Central Universities of Harbin Institute of Technology.

Electronic Supplementary Material Supplementary material is available in the online version of this article at https://dx.doi.org/10.1007/s11705-022-2155-1 and is accessible for authorized users.

References

1. Li J, Michalkiewicz B, Min J, Ma C, Chen X, Gong J, Mijowska E, Tang T. Selective preparation of biomass-derived porous carbon with controllable pore sizes toward highly efficient CO_2 capture. Chemical Engineering Journal, 2019, 360: 250–259
2. Kierzkowska A M, Pacciani R, Müller C R. CaO-based CO_2 sorbents: from fundamentals to the development of new, highly effective materials. ChemSusChem, 2013, 6(7): 1130–1148
3. Wang S, Li X, Wu H, Tian Z, Xin Q, He G, Peng D, Chen S, Yin Y, Jiang Z, Guiver M D. Advances in high permeability polymer-based membrane materials for CO_2 separations. Energy & Environmental Science, 2016, 9(6): 1863–1890
4. Du N, Park H B, Dal-Cin M M, Guiver M D. Advances in high permeability polymeric membrane materials for CO_2 separations. Energy & Environmental Science, 2012, 5(6): 7306–7322
5. Yu Q, Delgado J P, Veneman R, Brilman D W F. Stability of a benzyl amine based CO_2 capture adsorbent in view of regeneration strategies. Industrial & Engineering Chemistry Research, 2017, 56(12): 3259–3269
6. Li X, Hou M, Zhang Z, Han B, Yang G, Wang X, Zou L. Absorption of CO_2 by ionic liquid/polyethylene glycol mixture and the thermodynamic parameters. Green Chemistry, 2008, 10(8): 879–884
7. Lee Z H, Lee K T, Bhatia S, Mohamed A R. Post-combustion carbon dioxide capture: evolution towards utilization of nanomaterials. Renewable & Sustainable Energy Reviews, 2012, 16(5): 2599–2609
8. Yaumi A L, Bakar M Z A, Hameed B H. Recent advances in functionalized composite solid materials for carbon dioxide capture. Energy, 2017, 124: 461–480
9. Li D, Chen Y, Zheng M, Zhao H, Zhao Y, Sun Z. Hierarchically structured porous nitrogen-doped carbon for highly selective CO_2 capture. ACS Sustainable Chemistry & Engineering, 2016, 4(1): 298–304
10. Qie Z, Sun F, Gao J, Pi X, Wang L, Liu M, Qu Z, Zhao G. Enhanced SO_2 fluidized adsorption dynamic by hierarchically porous activated coke. Journal of the Energy Institute, 2020, 93(2): 802–810
11. Kim J, Lin L C, Swisher J A, Haranczyk M, Smit B. Predicting large CO_2 adsorption in aluminosilicate zeolites for postcombustion carbon dioxide capture. Journal of the American Chemical Society, 2012, 134(46): 18940–18943
12. Al-Maythalony B A, Shekhah O, Swaidan R, Belmabkhout Y, Pinnau I, Eddaoudi M. Quest for anionic MOF membranes: continuous sod-ZMOF membrane with CO_2 adsorption-driven selectivity. Journal of the American Chemical Society, 2015,

137(5): 1754–1757

13. Qi G, Wang Y, Estevez L, Duan X, Anako N, Park A H A, Li W, Jones C W, Giannelis E P. High efficiency nanocomposite sorbents for CO_2 capture based on amine-functionalized mesoporous capsules. Energy & Environmental Science, 2011, 4(2): 444–452
14. Oginni O, Singh K, Oporto G, Dawson-Andoh B, McDonald L, Sabolsky E. Influence of one-step and two-step KOH activation on activated carbon characteristics. Bioresource Technology Reports, 2019, 7: 100266
15. Deng H, Li G, Yang H, Tang J, Tang J. Preparation of activated carbons from cotton stalk by microwave assisted KOH and K_2CO_3 activation. Chemical Engineering Journal, 2010, 163(3): 373–381
16. Oginni O, Singh K, Oporto G, Dawson-Andoh B, McDonald L, Sabolsky E. Effect of one-step and two-step H_3PO_4 activation on activated carbon characteristics. Bioresource Technology Reports, 2019, 8: 100307
17. Tseng R L. Physical and chemical properties and adsorption type of activated carbon prepared from plum kernels by NaOH activation. Journal of Hazardous Materials, 2007, 147(3): 1020–1027
18. Yue L, Xia Q, Wang L, Wang L, DaCosta H, Yang J, Hu X. CO_2 adsorption at nitrogen-doped carbons prepared by K_2CO_3 activation of urea-modified coconut shell. Journal of Colloid and Interface Science, 2018, 511: 259–267
19. Kim M J, Choi S W, Kim H, Mun S, Lee K B. Simple synthesis of spent coffee ground-based microporous carbons using K_2CO_3 as an activation agent and their application to CO_2 capture. Chemical Engineering Journal, 2020, 397: 125404
20. Deng S, Wei H, Chen T, Wang B, Huang J, Yu G. Superior CO_2 adsorption on pine nut shell-derived activated carbons and the effective micropores at different temperatures. Chemical Engineering Journal, 2014, 253: 46–54
21. Rashidi N A, Yusup S. An overview of activated carbons utilization for the post-combustion carbon dioxide capture. Journal of CO_2 Utilization, 2016, 13: 1–16
22. Jagiello J, Kenvin J, Celzard A, Fierro V. Enhanced resolution of ultra micropore size determination of biochars and activated carbons by dual gas analysis using N_2 and CO_2 with 2D-NLDFT adsorption models. Carbon, 2019, 144: 206–215
23. Feng S, Li W, Shi Q, Li Y, Chen J, Ling Y, Asiri A M, Zhao D. Synthesis of nitrogen-doped hollow carbon nanospheres for CO_2 capture. Chemical Communications, 2014, 50(3): 329–331
24. Kim J, Han J, Ha D, Kang S. Synthesis of nitrogen and boron co-doped carbon (CNB) and their CO_2 capture properties: from porous to hollow granule structure. Journal of Materials Chemistry A, 2014, 2(39): 16645–16651
25. He X, Zhang H, Zhang H, Li X, Xiao N, Qiu J. Direct synthesis of 3D hollow porous graphene balls from coal tar pitch for high performance supercapacitors. Journal of Materials Chemistry A, 2014, 2(46): 19633–19640
26. Alabadi A, Razzaque S, Yang Y, Chen S, Tan B. Highly porous activated carbon materials from carbonized biomass with high CO_2 capturing capacity. Chemical Engineering Journal, 2015, 281: 606–612
27. Qie Z, Zhang Z, Sun F, Wang L, Pi X, Gao J, Zhao G. Effect of pore hierarchy and pore size on the combined adsorption of SO_2 and toluene in activated coke. Fuel, 2019, 257: 116090
28. Deng S, Hu B, Chen T, Wang B, Huang J, Wang Y, Yu G. Activated carbons prepared from peanut shell and sunflower seed shell for high CO_2 adsorption. Adsorption, 2015, 21(1-2): 125–133
29. Li D, Zhou J, Wang Y, Tian Y, Wei L, Zhang Z, Qiao Y, Li J. Effects of activation temperature on densities and volumetric CO_2 adsorption performance of alkali-activated carbons. Fuel, 2019, 238: 232–239
30. Liu J, Liu X, Sun Y, Sun C, Liu H, Stevens L A, Li K, Snape C E. High density and super ultra-microporous-activated carbon macrospheres with high volumetric capacity for CO_2 capture. Advanced Sustainable Systems, 2018, 2(2): 1700115
31. Haffner-Staton E, Balahmar N, Mokaya R. High yield and high packing density porous carbon for unprecedented CO_2 capture from the first attempt at activation of air-carbonized biomass. Journal of Materials Chemistry A, 2016, 4(34): 13324–13335
32. Guo L, Yang J, Hu G, Hu X, Wang L, Dong Y, DaCosta H, Fan M. Role of hydrogen peroxide preoxidizing on CO_2 adsorption of nitrogen-doped carbons produced from coconut shell. ACS Sustainable Chemistry & Engineering, 2016, 4(5): 2806–2813
33. Fan Z, Cheng Z, Feng J, Xie Z, Liu Y, Wang Y. Ultrahigh volumetric performance of a free-standing compact N-doped holey graphene/PANI slice for supercapacitors. Journal of Materials Chemistry A, 2017, 5(32): 16689–16701
34. Wang L, Sun F, Gao J, Pi X, Pei T, Qie Z, Zhao G, Qin Y. A novel melt infiltration method promoting porosity development of low-rank coal derived activated carbon as supercapacitor electrode materials. Journal of the Taiwan Institute of Chemical Engineers, 2018, 91: 588–596
35. Kommu A, Singh J K. Separation of ethanol and water using graphene and hexagonal boron nitride slit pores: a molecular dynamics study. Journal of Physical Chemistry C, 2017, 121(14): 7867–7880
36. Zhou H, Xie J, Liu B, Ban S. Molecular simulation of methane adsorption in activated carbon: the impact of pore structure and surface chemistry. Molecular Simulation, 2016, 42(9): 776–782
37. Malde A K, Zuo L, Breeze M, Stroet M, Poger D, Nair P C, Oostenbrink C, Mark A E. An automated force field topology builder (ATB) and repository: version 1.0. Journal of Chemical Theory and Computation, 2011, 7(12): 4026–4037
38. Miller D L, Kubista K D, Rutter G M, Ruan M, De Heer W A, Kindermann M, First P N, Stroscio J A. Real-space mapping of magnetically quantized graphene states. Nature Physics, 2010, 6(10): 811–817
39. Qie Z, Sun F, Zhang Z, Pi X, Qu Z, Gao J, Zhao G. A facile trace potassium assisted catalytic activation strategy regulating pore topology of activated coke for combined removal of toluene/SO_2/NO. Chemical Engineering Journal, 2020, 389: 124262
40. Wang L, Sun F, Hao F, Qu Z, Gao J, Liu M, Wang K, Zhao G, Qin Y. A green trace K_2CO_3 induced catalytic activation strategy for developing coal-converted activated carbon as advanced candidate for CO_2 adsorption and supercapacitors. Chemical

Engineering Journal, 2020, 383: 123205

41. Sun F, Gao J, Yang Y, Zhu Y, Wang L, Pi X, Liu X, Qu Z, Wu S, Qin Y. One-step ammonia activation of Zhundong coal generating nitrogen-doped microporous carbon for gas adsorption and energy storage. Carbon, 2016, 109: 747–754
42. Plaza M G, González A S, Pis J J, Rubiera F, Pevida C. Production of microporous biochars by single-step oxidation: effect of activation conditions on CO_2 capture. Applied Energy, 2014, 114: 551–562
43. Vargas D P, Giraldo L, Erto A, Moreno-Piraján J C. Chemical modification of activated carbon monoliths for CO_2 adsorption. Journal of Thermal Analysis and Calorimetry, 2013, 114(3): 1039–1047
44. Zhu X L, Wang P Y, Peng C, Yang J, Yan X B. Activated carbon produced from paulownia sawdust for high-performance CO_2 sorbents. Chinese Chemical Letters, 2014, 25(6): 929–932
45. Plaza M G, González A S, Pevida C, Pis J J, Rubiera F. Valorisation of spent coffee grounds as CO_2 adsorbents for postcombustion capture applications. Applied Energy, 2012, 99: 272–279
46. Parshetti G K, Chowdhury S, Balasubramanian R. Biomass derived low-cost microporous adsorbents for efficient CO_2 capture. Fuel, 2015, 148: 246–254
47. Wang J, Heerwig A, Lohe M R, Oschatz M, Borchardt L, Kaskel S. Fungi-based porous carbons for CO_2 adsorption and separation. Journal of Materials Chemistry, 2012, 22(28): 13911–13913
48. Sevilla M, Fuertes A B. Sustainable porous carbons with a superior performance for CO_2 capture. Energy & Environmental Science, 2011, 4(5): 1765–1771
49. Silvestre-Albero A, Silvestre-Albero J, Martínez-Escandell M, Rodríguez-Reinoso F. Micro/mesoporous activated carbons derived from polyaniline: promising candidates for CO_2 adsorption. Industrial & Engineering Chemistry Research, 2014, 53(40): 15398–15405
50. Wang L, Sun F, Gao J, Zhu Y, Pei T, Li L, Zhao G, Qin Y. Pore reorganization of porous carbon during trace calcium-catalyzed coal activation for adsorption applications. Energy & Fuels, 2018, 32(9): 9191–9201